**SANDIA REPORT**
SAND2010-5963
Unlimited Release
Printed September 2010

# Influence of the Richtmyer-Meshkov Instability on the Kinetic Energy Spectrum

Christopher R. Weber

Prepared by
Sandia National Laboratories
Albuquerque, New Mexico 87185 and Livermore, California 94550

Sandia National Laboratories is a multi-program laboratory managed and operated by Sandia Corporation, a wholly owned subsidiary of Lockheed Martin Corporation, for the U.S. Department of Energy's National Nuclear Security Administration under contract DE-AC04-94AL85000.



Issued by Sandia National Laboratories, operated for the United States Department of Energy by Sandia Corporation.



Available to DOE and DOE contractors from
U.S. Department of Energy
Office of Scientific and Technical Information
P.O. Box 62
Oak Ridge, TN 37831

Telephone: (865) 576-8401
Facsimile: (865) 576-5728
E-Mail: reports@adonis.osti.gov
Online ordering: http://www.osti.gov/bridge

Available to the public from
U.S. Department of Commerce
National Technical Information Service
5285 Port Royal Rd.
Springfield, VA 22161

Telephone: (800) 553-6847
Facsimile: (703) 605-6900
E-Mail: orders@ntis.fedworld.gov
Online order: http://www.ntis.gov/help/ordermethods.asp?loc=7-4-0#online

SAND2010-5963
Unlimited Release
Printed September 2010

# Influence of the Richtmyer-Meshkov Instability on the Kinetic Energy Spectrum

Christopher R. Weber
University of Wisconsin-Madison
1500 Engineering Drive
Madison, WI 53706

## Abstract

The fluctuating kinetic energy spectrum in the region near the Richtmyer-Meshkov instability (RMI) is experimentally investigated using particle image velocimetry (PIV). The velocity field is measured at a high spatial resolution in the light gas to observe the effects of turbulence production and dissipation. It is found that the RMI acts as a source of turbulence production near the unstable interface, where energy is transferred from the scales of the perturbation to smaller scales until dissipation. The interface also has an effect on the kinetic energy spectrum farther away by means of the distorted reflected shock wave. The energy spectrum far from the interface initially has a higher energy content than that of similar experiments with a flat interface. These differences are quick to disappear as dissipation dominates the flow far from the interface.

# Contents

# Figures

## Acronyms

| | |
|---|---|
| DFT | Discrete Fourier Transform |
| CCD | Charge Coupled Device |
| ICF | Inertial Confinement Fusion |
| PIV | Particle Image Velocimetry |
| RMI | Richtmyer-Meshkov Instability |
| RTI | Rayleigh-Taylor Instability |

# Influence of the Richtmyer-Meshkov Instability on the Kinetic Energy Spectrum

## 1.0 Introduction

The Richtmyer-Meshkov instability (RMI) [1, 2] occurs when a shock wave passes through an interface separating a pair of gases. Any perturbation on that interface is unstable to the shock acceleration and will grow in amplitude. If the amplitude is much less than the wavelength, the growth is linear and given by the equation

$$\dot{\eta} = kA^{+}V_0\eta_0^{+}, \qquad (1)$$

where $k$ is the wavenumber, $A = (\rho_2 - \rho_1)/(\rho_2 + \rho_1)$ is the Atwood number, $V_0$ is the velocity of an unperturbed interface after acceleration by the shock wave, and $\eta_0$ is the initial amplitude. The superscript "+" denotes post-shocked quantities.

RMI studies typically investigate the growth of the perturbation (for examples, see the review article by Bouillette [3]). Some effort has been made to study the turbulence that results from this perturbation growth. Laser doppler anemometry measurements have characterized the fluctuations inside the turbulent mixing zone, where dissipation and diffusion reduce the magnitude of the fluctuations but expand the spatial extent of this zone [4]. The mixing within a shocked gas-curtain showed that a late time transition to Kolmogorov scaling occurs [5,6]. The energy transfer within the Rayleigh-Taylor instability (RTI) was studied through direct numerical simulations [7], showing that energy is initially concentrated in scales corresponding to the dominant wavelength and spreads out to larger wavenumbers as vortex stretching and bending transfer energy to smaller scales.

A description of the energy scales in the RMI and how they vary in space and time is important to applications in inertial confinement fusion (ICF) and shock-induced mixing from supernova explosions. Simulations in these areas often use subgrid-scale models [8,9] to approximate the energy transfer to and from unresolved scales. These models rely on coefficients that need to be set to provide the best description of the underlying physics. An additional consideration, particularly in ICF, is the far-field effect of the instability. If the presence of a perturbation on the interface is felt far from the interface, it can have an influence on fusion ignition and burn wave propagation. This influence begins with the distorted transmitted shock wave converging to the capsule center.

When the shock wave passes from a light gas to a heavy gas, a reflected shock wave will propagate away from the interface through the light gas. This reflected shock wave initially takes on the distorted shape of the perturbed interface and, as it returns to planar, will leave a wake behind. This occurs because the concave portion of the distorted shock wave will converge slightly and strengthen. With the two refracted (transmitted and reflected) shock waves, the effect of the interface is felt far from the interface.

The interaction of the shock wave with the gas far from the interface can be described as being similar to the shock-turbulence interaction, where a shock wave passing through a turbulent field

will amplify any existing turbulence in the flow [10]. In RMI experiments, any background turbulence present in the shock tube will also be amplified. In addition, the shock will interact differently with the longitudinal and transverse components, leaving behind an anisotropic turbulent field. After the interaction, without any additional production of turbulence, the turbulence will return to isotropic and decay through dissipation [11].

Additional production of turbulence, however, can be found near the interface of the RMI. A turbulent viscosity model [11] has the production term

$$P = \nu_T \frac{dU_1}{dx_2} . \tag{2}$$

The velocity gradients from the interfacial perturbation growth act as a source of turbulence that transfers to smaller length scales. The fluctuating kinetic energy spectrum initially contains energy at the large scales approximately equal to the wavelength of the perturbation. After some time, the spectrum will have filled out to the inertial sub-range, and then to the dissipation range. Cook and Zhou [7] described the energy spectrum in the RTI and showed that the dominant wavelength initially had the bulk of the kinetic energy, but as the instability developed the spectrum filled out to larger (due to bubble merger) and smaller scales. The main difference between the energy in the RTI and the RMI is that the former is continuously forced by the sustained acceleration field while the latter only has the energy left behind by the shock wave.

The perturbation growth and the interaction of the distorted shock wave with the surrounding gas leads to several turbulence mechanisms operating at different scales, locations, and times. The work discussed here analyzes the energy spectra at two times and at two locations with respect to the interface. The location further from the interface is considered similar to that of the shock-turbulence interaction, where dissipation and return to isotropy are the two processes that can be expected to occur. The turbulence at the location near the interface is expected to experience the additional production mechanism of the RMI perturbation growth.

## 2.0 Experimental Setup

The experiments are performed at the Wisconsin Shock Tube Laboratory [12]. The shock tube is a downward firing, 9.13 m vertical tube. The driver has a circular cross section with a 0.41 m radius and a 2.08 m length while the driven section has a square cross section with 0.25 m sides. A high-pressure boost tank is connected to the driver section by a pneumatically-driven fast-opening valve to control the diaphragm rupture time. Piezoelectric pressure transducers mounted along the shock tube side walls are used to trigger the controlling electronics and to measure the shock wave speed.

A $N_2$-$SF_6$ interface is created by flowing $N_2$ from the top of the shock tube and $SF_6$ from the bottom. Slots, located 1 m from the bottom of the shock tube, allow a stagnation plane to form and excess gas to be removed with the aid of a vacuum pump. The slots are centered in a pair of $5.08 \times 25.4$ cm$^2$ rectangular pistons that are embedded in the wall of the shock tube wall. After the gases have flowed for a sufficient time to ensure purity, the pistons are oscillated at 3.27 Hz for 10 revolutions to create a 2-dimensional standing wave with an initial amplitude of 0.38 cm and a wavelength of 9.1 cm. An example of this initial condition is shown in Figure 1. The Atwood number of the interface is 0.68 initially and 0.77 after being compressed by the shock wave.

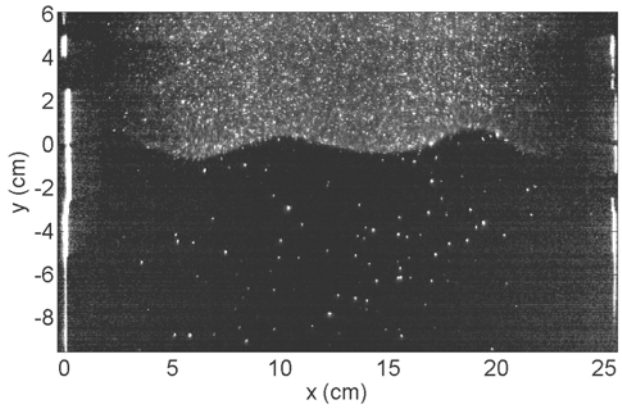


**Figure 1: Initial condition.** The $N_2$-$SF_6$ interface with the waveform initial condition is shown just prior to being accelerated by a shock wave. The $N_2$ is seeded with $Al_2O_3$ particles.

Prior to the experiment, the driver section is filled to 90% of the diaphragm rupture pressure. Excess pressure is then released into the driver using fast-opening valves that are timed in relation to the standing wave, rupturing the diaphragm and launching a shock wave towards the interface. The shock wave has an incident Mach number of $M$=2.05 and the post-shocked interface velocity is 298 m/s.

Flow visualization is performed by seeding the $N_2$ with $Al_2O_3$ particles using a TSI fluidized bed (model 3400). Particles are mixed with the flow for approximately a minute prior to the experiment, allowing for a uniform particle distribution to be observed. Planar images are obtained using two lasers and three cameras. The initial condition is illuminated using a continuous $Ar^+$ laser of approximately 1W in power and spread into a sheet with a cylindrical lens. A high speed camera, IDT model XS4, is set up at the location of the stagnation plan to record the standing wave being created and determine the final interface shape before the shock

reaches the interface. The post-shocked interface is recorded using two cameras and a dual-cavity Nd-YAG laser. The two pulses from the Nd-Yag laser are spaced 14 μs apart and have a pulse duration of ~10 ns. A LaVision Flowmaster 2 camera is focused onto a 2.2 cm x 2.8 cm region and records two images corresponding to each of the Nd-YAG pulses. A thermoelectrically cooled Andor CCD camera is mounted at an angle to the image plane to accommodate the LaVision camera, and provides a full-field view of the interface. The slow shutter on this camera requires that both Nd-YAG pulses are captured on a single image. Both cameras have a 532 nm laser line filter to allow only the light from the Nd-YAG laser.

Images obtained from two experiments are shown in Figure 2; each image was taken with the full-field camera and the rectangular boxes show the regions that the zoomed-in camera is focused on. The obstruction in the right half of the image is the LaVision camera. These images are taken at 0.3 ms and 1.0 ms after the shock wave accelerates the interface and the locations are 5 cm and 9 cm away from the interface at both times.

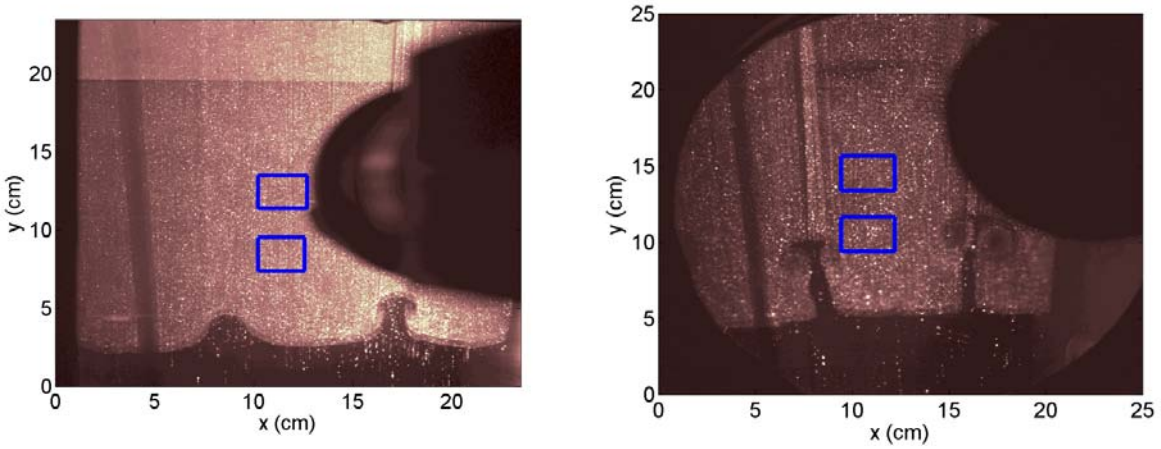


**Figure 2: Post-shocked interface and regions of interest.** These images are taken with the full-field camera at 0.3 ms and 1.0 ms showing the post-shocked interface with an initial waveform perturbation. The blue boxes show the regions that the PIV camera (black obstruction in the right half of the image) is focused on.

The pair of zoomed-in images is analyzed using particle image velocimetry (PIV) to obtain a velocity field. The mean flow has displaced 200 pixels between the two images, allowing small differences in the velocity field to be measured. The first step in the PIV analysis is to remove the background by subtracting a median filtered image from the original image. The background subtraction helps remove a zero-displacement bias of the cross-correlation procedure. The two images are shifted by the estimated mean displacement and a cross-correlation analysis is applied to 64x64 pixel regions across the image to obtain the displacement field. The sub-pixel displacement is determined by assuming the cross-correlation matrix has a Gaussian shape and interpolating to find its peak location [13]. The displacement field is then filtered to remove spurious vectors and smoothed. The two images are then deformed using this displacement field and a bilinear interpolation algorithm. The first image is deformed by half the displacement field and the second is deformed in the opposite direction by half the displacement field, ideally resulting in two images with identical particle locations. A cross-correlation analysis is then applied to the deformed image. This process of image deformation and cross-correlation is iterated, without the smoothing step, until the deformed images have a negligibly small

displacement field. This iteration occurred four times with a decreasing window size and increasing overlap, reaching a final size of 32x32 pixels with 50% overlap. This iterative image deformation method has been shown to improve the precision of sub-pixel displacement measurements by an order of magnitude over cross-correlation methods without image deformation [14,15].

An example of a velocity field from PIV is shown in Figure 3(a) from a late time image far from the interface which corresponds to the upper rectangular box in Figure 2 (b). The mean velocity of 298.2 m/s is removed, showing the fluctuating field. A reference vector of 5 m/s is shown in the upper right of the image and Figure 3(b) shows the magnitude of the velocity. The spatial resolution of the velocity field is 335 μm. The turbulent intensity, defined as

$$I = \frac{\sqrt{\langle u^2 \rangle}}{U}, \tag{3}$$

averaged over all of the experiments is 0.59% in the streamwise direction and 0.87% in the transverse direction. A conservative estimate of PIV measurement error of 0.1 pixel displacement would correspond to 0.15 m/s which would change the turbulent intensity by 0.05%.

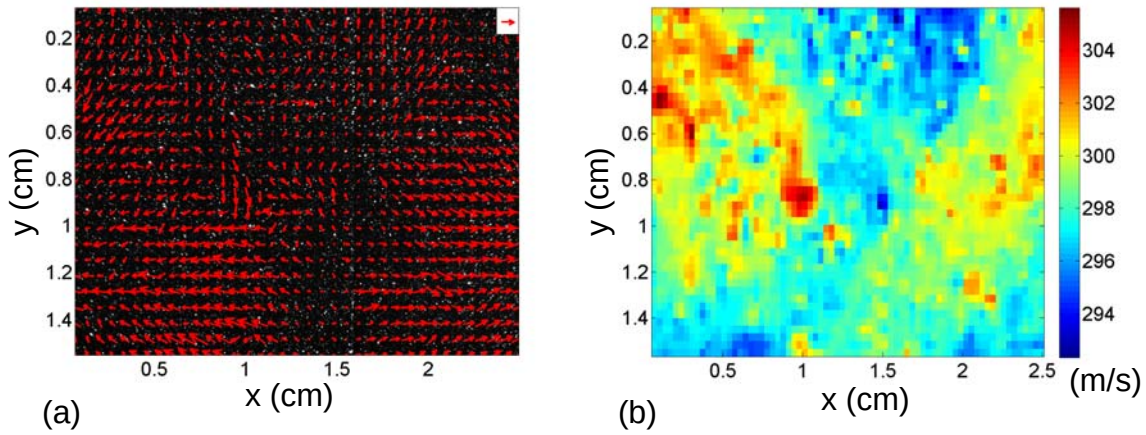


**Figure 3: PIV results.** (b) The vector field from a PIV analysis with the mean velocity subtracted. The reference vector in the top right corner is 5 m/s. The background is the original particle image. (b) The velocity magnitude of the image in (a).

The second source of error comes from the ability of the particles to track the flow. The particles have a stated size of 50 nm but may agglomerate to sizes much larger than this [16]. A way of indirectly determining the particle size is by observing the lag distance behind the flow. Figure 4 shows an experiment where the bottom gas was seeded and the shock wave impulsively accelerated the interface to 390 m/s. The image shows that, while there are a handful of particles that fell behind the interface by ~ 1 cm, the majority of the particles are within 0.25 cm of the interface. Using this distance in a Stokes drag calculation, a particle size of 1.1 μm is found. Hjelmfelt and Mockros [17] analyzed the ability of a particle to follow the turbulence of a given frequency. With this particle size, a maximum turbulence frequency of 27 kHz is observable. From the eddy turnover frequency, $u_k k/2\pi$, obtained from the energy spectra data that will be

discussed below, a maximum turbulent frequency of ~200 Hz is observed. Therefore these particles adequately follow all eddies in the post-shocked flow.

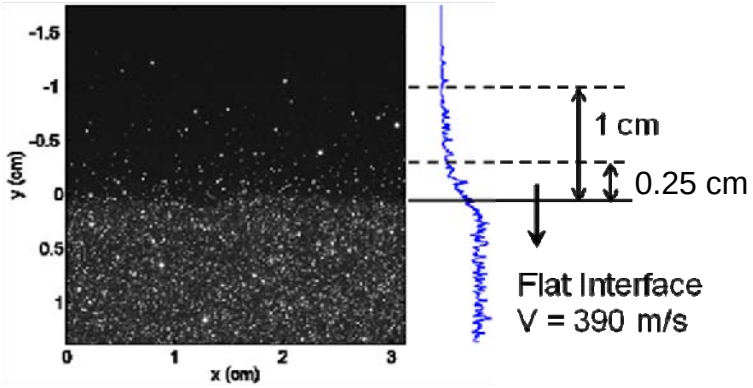


**Figure 4: Particle lag after an impulsive acceleration.** The initially flat interface was shock-accelerated to 390 m/s and some particles required a distance to accelerate to the gas velocity. Some particles are up to 1 cm behind the interface, while the majority of the particles are within 0.25 cm.

# 3.0 Fluctuating Kinetic Energy Spectra

The spectrum of turbulent kinetic energy is computed in both the *x* (transverse) and *y* (streamwise) directions. The procedure for the *x*-direction is as follows. The fluctuating velocity within a row of the velocity field data is obtained by subtracting off the mean velocity in this row. A discrete Fourier transform (DFT) of the fluctuating velocity is computed using a window function to reduce spectral leakage [18]. As in other experimental turbulence spectra measurements [19,20], a Hanning window function was chosen for computing the DFT. The total kinetic energy spectra is found by multiplying the transformed component by its complex conjugate and adding the energy from the other direction of velocity. An example of this energy spectrum is shown in the semi-log plot Figure 5, where the *x*-axis is the log of the wavenumber and the *y*-axis is the location of each row. This plot shows that the spectrum does change significantly throughout the domain. Each spectral component is averaged across the domain and combined with that of two other experiments of the same type (same time, location, and initial interface).

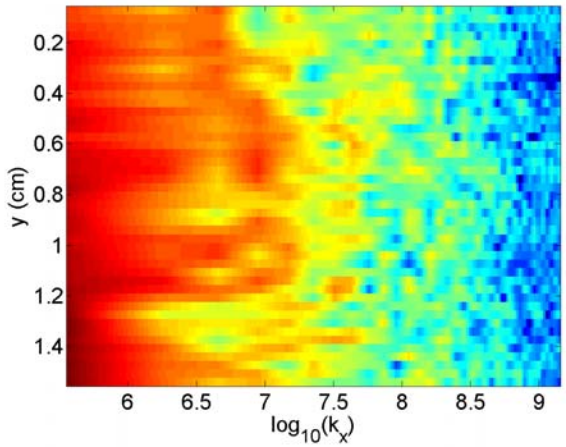


**Figure 5: Semi-log plot of fluctuating kinetic energy.** The *y*-axis is the physical dimension in the PIV image and the x-axis is log of the wavenumber. The energy spectrum does not change significantly throughout the height of the domain.

As already mentioned, data is taken at two times, referred to as early and late, and at two locations, referred to as near and far with respect to the interface. The experiments are conducted with an initial sinusoidal waveform imposed on the interface and with an initially flat interface, referred to as wave and flat experiments, respectively. Three experiments were conducted for each of these eight different scenarios, with a total of 24 experiments in all. The spectra shown in the following figures are averages from the three experiments.

Figure 6 shows the fluctuating kinetic energy spectra at the early time. The error bars represent the 95% confidence interval for the mean energy at that wavenumber across the entire velocity field from the three experiments of the same type. For most wavenumbers in the spectra, the $k_y$ modes have a higher energy content than the $k_x$ modes. This is true for both the initially flat interface and that with a waveform perturbation. This shows the anisotropy of the post-shocked turbulence. Because the turbulence is anisotropic, we do not expect a $k^{-5/3}$ scaling. The spectra have a slightly lower slope than -5/3 up until about $4 \times 10^3$ $m^{-1}$, after which the slope is steeper,

possibly signifying the beginning of the dissipative range. Since the initial turbulence spectrum is not known, the anisotropy may be due to the shock wave or the initial spectrum.

Near the interface in these early time experiments, the first few lower wavenumber modes in the $k_x$ direction have a higher energy content when the waveform is present on the interface. In the $k_y$ direction, and at higher wavenumber in the $k_x$ direction, the flat interface spectra have a slightly higher energy content when compared to waveform experiments. The reason for these differences is not clear. Further from the interface the spectra from the interface with an initial wave perturbation have a higher energy content than that of the initially flat interface. A possible explanation for this is that the region further from the interface has more recently experienced a shock wave passing through it. The shock wave that reflects off the interface is deformed with a shape similar to the interface and distorts the flow field behind it as it returns to planar. The near location has had more time for these effects to dissipate away. It can also be seen that the spectra at the far location are larger in magnitude than that of the near location at this early time, which also suggests that dissipation is behind these differences. From this, we can expect that the differences in the far location will become less at later times.

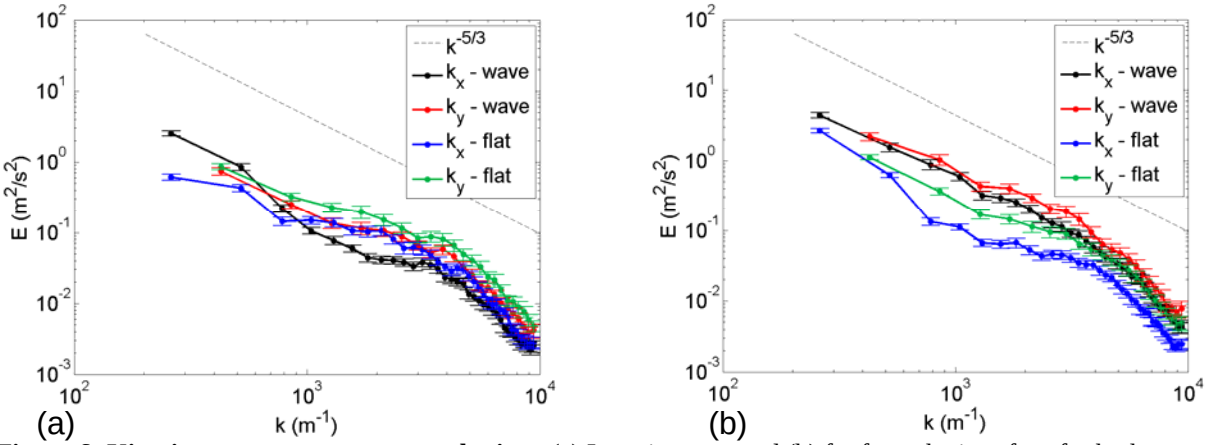


**Figure 6: Kinetic energy spectrum at early time.** (a) Location near and (b) far from the interface for both an interface with a waveform perturbation and a flat interface. The error bars signify the 95% confidence interval for the mean values.

The fluctuating kinetic spectra for the later time experiments are shown in Figure 7. In Figure 7(b), we see that, as expected, the differences in the kinetic energy spectra are reduced: the spectra from the experiments with an initial wave are nearly the same as that from the flat interface experiments. The $k_y$ spectra are still larger than the $k_x$ spectra so it appears that a return to isotropy will occur at larger times scales than are observed between these experiments. At the nearer location the spectra for the wavy interface in both directions are larger than those for the flat interface. The spectra in Figure 7(a) do not extend to the high wavenumbers that are obtained in the rest of the experiments because the PIV interrogation window size was doubled. At this location it appears that mixing between the two gases and boundary layer effects are causing refractive index gradients, known as aero-optical effects [21], to blur the image slightly, so a larger interrogation window was needed to include enough clear particles to get an accurate velocity measurement.

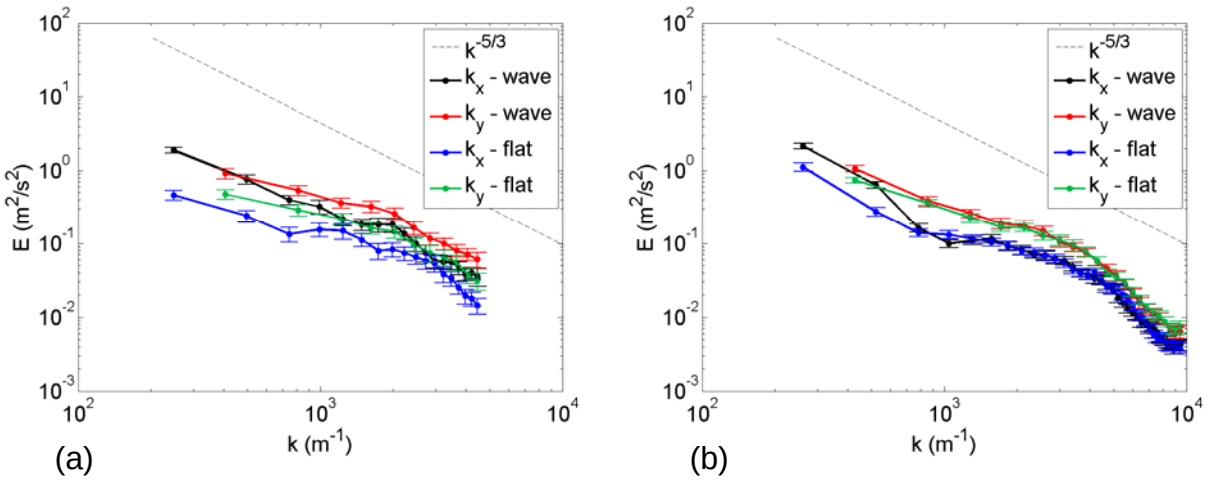


**Figure 7: Kinetic energy spectrum at late time.** (a) Location near and (b) far from the interface for both an interface with a waveform perturbation and a flat interface.

The change in the spectra over time is shown by combining Figure 6 and 7. Figure 8(a) shows that near the perturbed interface, the spectra at higher wavenumbers increase in energy content between the early and late times. At the location further from the interface, Figure 8(b), the energy content at all wavenumbers decreased from the early to the late time. These spectra seem to confirm our hypothesis, that the deforming interface will add kinetic energy near to it, while dissipation will dominate further from the interface.

Near the flat interface, Figure 9, the energy spectra stay nearly the same, decreasing slightly for a few wavenumbers. Far from the flat interface the spectra also stay roughly the same; the $k_x$ spectra increases slightly at high wavenumber and decreases slightly at low wavenumbers. It was expected that a decrease in the energy spectra would have been observed in these figures, similar to that of Figure 8(b). What appears to be occurring is that the excess energy left behind by the distorted shock wave is quickly dissipated away. This rate of energy dissipation is higher than the dissipation of the initial turbulence, which is presumably present in the flat interface spectra and does not change significantly.

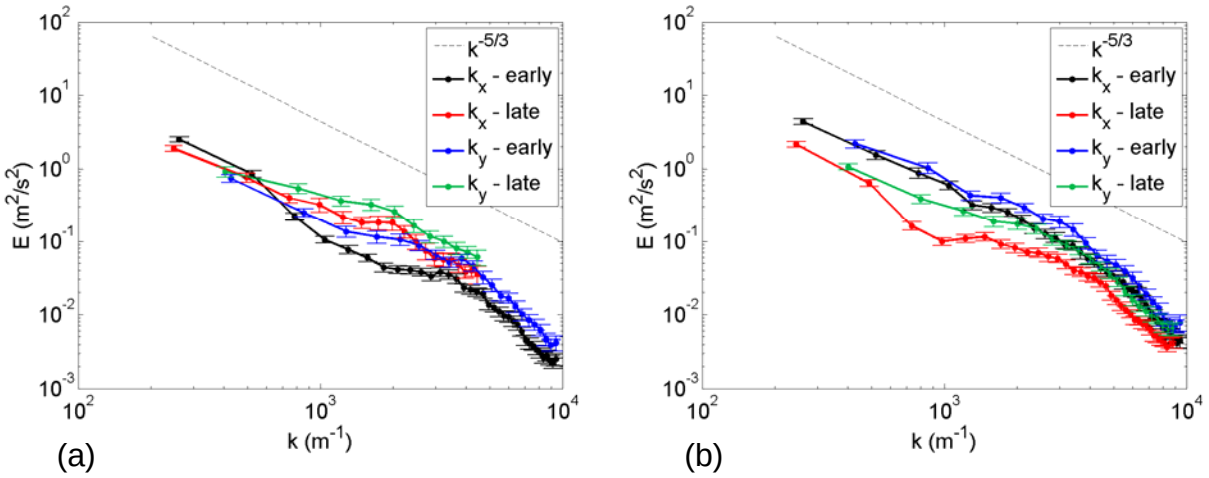


**Figure 8: Kinetic energy spectra for wave interface.** The spectra at different times are compared at the (a) near and (b) far locations.

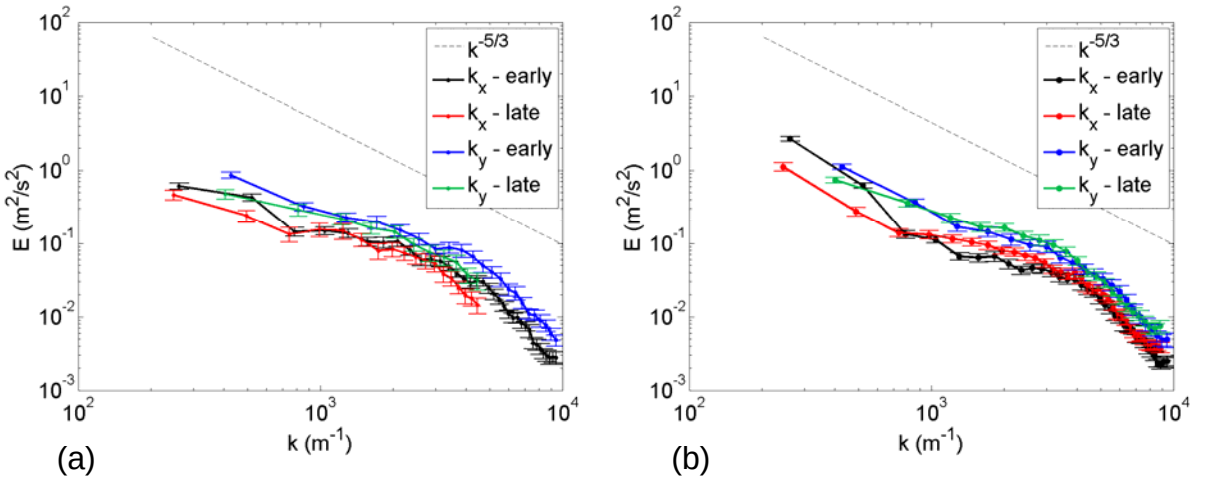


**Figure 9: Kinetic energy spectra for flat interface.** The spectra at different time are compared at the (a) near and (b) far locations.

# 4.0 Simulation

To confirm the trends discussed in these experiments, a single mode, two-dimensional simulation was preformed. The initial conditions in the simulation were set to match the initial Mach number, wavelength and amplitude of the experiment. No initial velocity, other than the shocked gas, was present in the initial setup. The simulation uses 10th order spatial differencing with a 4th order Runge-Kutta temporal integration. An artificial fluid large eddy simulation (LES) scheme is used to provide stability along with the appropriate numerical dissipation [22]. The resolution in the simulation is  /256 = 348 μm, providing a similar resolution to the PIV data.

The fluctuating energy spectra are computed in regions chosen to be a similar distance from the interface as the locations observed in the experiments. The red region in Figure 10 spans the entire width of the domain. Since the *x*-boundaries in the simulation are periodic, the spectra in this region can be computed without the use of a window function. The green region is chosen to be the same size and location as in the experiments, but it is necessary to use a Hanning window function when computing the DFT.

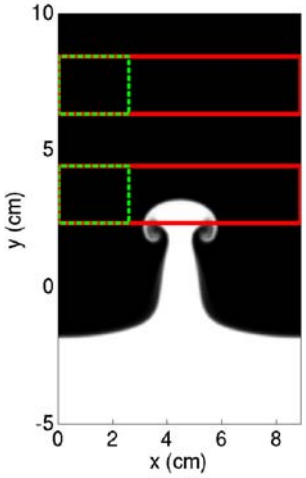


**Figure 10: Analysis regions in simulation.** A field plot of $N_2$ (black) and $SF_6$ (white) is plotted from the simulation at 0.9 ms and the two analysis regions are shown. The Fourier transform in the full width of the domain (red) allows us to take advantage of the periodic boundary conditions. The green region is chosen to match the region investigated in the experiment.

Figure 11 show the spectra computed using the full width of the domain. The trends of interest in these spectra are an increase in spectral energy at the near location and a decrease in energy far from the interface. These trends appear to be present for most wavenumbers. A hump in the spectrum is present at the earliest time near $k_x$ = 2000 $m^{-1}$ at both locations and dissipates away. It is not clear where this feature comes from. Since the simulation is 2-dimensional, a $k^{-3}$ spectrum is expected for fully developed turbulence [23] and is observed at the later time near the interface.

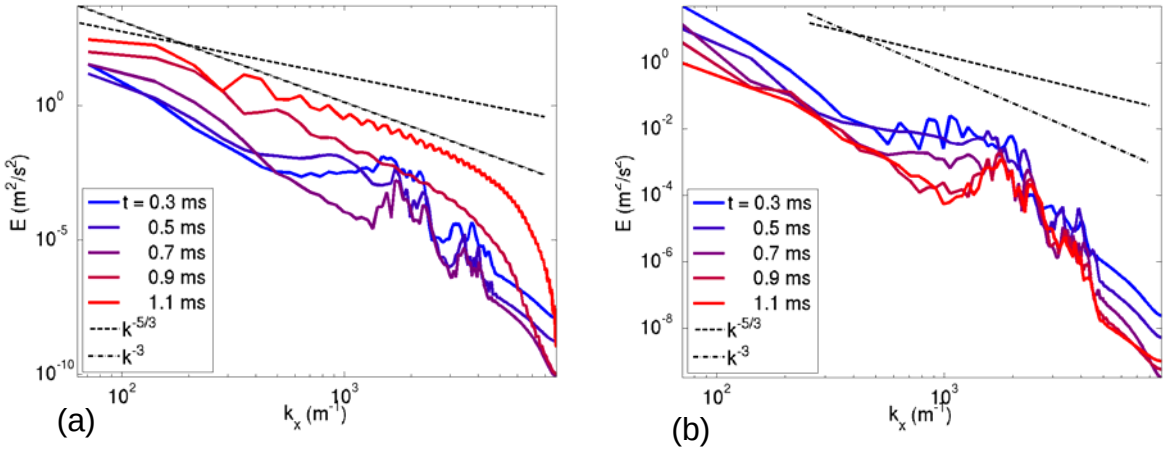


**Figure 11: Kinetic energy spectra from simulation using full domain width.** Five energy spectra are plotted from different times to show changes (a) near and (b) far from the interface.

Figure 12 shows the spectra computed within the green box in Figure 10 and using a Hanning window function. Near the interface at this location the energy spectra decrease for the first few time steps and then increase over the last three times. The hump in the spectra is also present at this location and is gone by the later times. Further from the interface, nearly all modes decrease in energy at each time step.

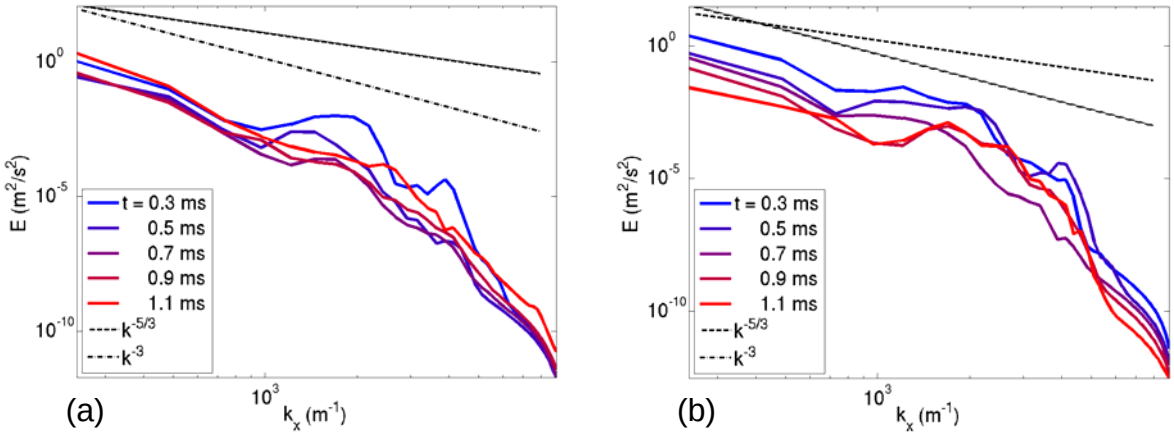


**Figure 12: Kinetic energy spectra from the simulation using the smaller region.** The smaller region of interest (a) near and (b) far from the interface is chosen to match the location observed in the experiments. The energy spectra from five times are shown.

The simulation data appear to confirm the results shown in the experiments, that energy production occurs near the interface and dissipation dominates further from the interface. A 3-dimensional simulation is necessary to make quantitative comparisons to the experiments, as the physics of the energy cascade are fundamentally different in three dimensions. At the present time, a 3-D simulation has not been computed because of the significant computational cost required to resolve the necessary scales.

# 5.0 Summary and Discussion

This work investigated the energy spectra at small scales in the presence of a shock-accelerated interface and the effect that the Richtmyer-Meshkov instability has on the spectra. It is observed that, near the perturbation, the energy spectra increase in time as energy from the large scales of the perturbation cascades towards smaller scales. Further from the interface the presence of the perturbation is observed, as the fluctuating kinetic energy is higher than that of a flat interface. Later in time these differences are no longer present, as dissipation has reduced the excess energy deposited by the distorted reflected shock wave.

It is unclear as to why the spectra with a flat interface stay largely unchanged between the two times. It is possible that dissipation effects will be enhanced and more easily observed in a flow with higher turbulence intensity. When the flow becomes isotropic is not known and experiments later in time are needed to investigate this.

This is, as far as the author is aware, the first time that the influence of the RMI on the kinetic energy spectrum has been experimentally investigated at different locations from the interface. Since this influence extends beyond just the mixing region, it is possible that applications concerned with the RMI will need to consider more than just the mixing width.

# 6.0 References


[1] Richtmyer, R.D. (1960). Taylor instability in shock acceleration of compressible fluids. *Communications on Pure and Applied Mathematics*, 13(2):297-319.

[2] Meshkov, E.E. (1969). Instability of the interface of two gases accelerated by a shock wave. *Fluid Dynamics*, 4(5):101–104.

[3] Brouillette, M. (2002). The Richtmyer-Meshkov instability. *Annual Review of Fluid Mechanics*, 34, 445-468.

[4] Poggi, F., Thorembey, M. H., & Rodriguez, G. (1998). Velocity measurements in turbulent gaseous mixtures induced by Richtmyer-Meshkov instability. *Physics of Fluids*, 10, 2698-2700.

[5] Vorobieff, P., Rightley, P. M., & Benjamin, R. F. (1998). Power-law spectra of incipient gas-curtain turbulence. *Physical Review Letters*, 81(11), 2240-2243.

[6] Vorobieff, P., Mohamed, N. G., Tomkins, C., Goodenough, C., Marr-Lyon, M., & Benjamin, R. (2003). Scaling evolution in shock-induced transition to turbulence. *Physical Review E*, 68(6), 65301.

[7] Cook, A. W., & Zhou, Y. (2002). Energy transfer in Rayleigh-Taylor instability. *Physical Review E*, 66(2), 26312.

[8] Besnard, D. C., Harlow, F. H., Rauenzahn, R. M. and Zemach, C. (1992). Turbulence transport equations for variable-density turbulence and their relationship to two-field models, *LA-12303-MS*.

[9] Dimonte, G., & Tipton, R. (2006). KL turbulence model for the self-similar growth of the Rayleigh-Taylor and Richtmyer-Meshkov instabilities. *Physics of Fluids*, 18, 085101.

[10] Andreopoulos, Y., Agui, J. H., & Briassulis, G. (2000). Shock wave&-turbulence interactions. *Annual Review of Fluid Mechanics*, 32(1), 309-345.

[11] Pope, S. B. (2000). Turbulent flows *Cambridge Univ Pr*.

[12] Motl, B., Oakley, J., Ranjan, D., Weber, C., Anderson, M., & Bonazza, R. (2009). Experimental validation of a Richtmyer–Meshkov scaling law over large density ratio and shock strength ranges. *Physics of Fluids*, 21, 126102.

[13] Willert, C., & Gharib, M. (1991). Digital particle image velocimetry. *Experiments in Fluids*, 10(4), 181-193.

[14] Jambunathan, K., Ju, X., Dobbins, B., & Ashforth-Frost, S. (1995). An improved cross correlation technique for particle image velocimetry. *Measurement Science and Technology*, 6, 507.

[15] Scarano, F. (2002). Iterative image deformation methods in PIV. *Measurement Science and Technology*, 13, R1.

[16] Melling, A. (1997). Tracer particles and seeding for particle image velocimetry. *Measurement Science & Technology*, 8(12), 1406-1416.

[17] Hjelmfelt, A., & Mockros, L. (1966). Motion of discrete particles in a turbulent fluid. *Applied Scientific Research*, 16(1), 149-161.

[18] Harris, F. J. (1978). On the use of windows for harmonic analysis with the discrete Fourier transform. *Proceedings of the IEEE,* 66(1), 51-83.

[19] Doron, P., Bertuccioli, L., Katz, J., & Osborn, T. (2001). Turbulence characteristics and dissipation estimates in the coastal ocean bottom boundary layer from PIV data. *Journal of Physical Oceanography*, 31, 2108-2134.

[20] Tomkins, C., & Adrian, R. (2005). Energetic spanwise modes in the logarithmic layer of a turbulent boundary layer. *Journal of Fluid Mechanics*, 545, 141-162.

[21] Gilbert, K., & Otten, L. (1982). Aero-optical phenomena. *Progress in Astronautics and Aeronautics*, 80

[22] Cook, A. W. (2007). Artificial fluid properties for large-eddy simulation of compressible turbulent mixing. *Physics of Fluids*, 19, 055103.

[23] Kraichnan, R. H. (1967). Inertial ranges in Two-Dimensional turbulence. *Physics of Fluids*, 10, 1417.

## Distribution

1 Christopher Weber
University of Wisconsin-Madison
1500 Engineering Drive
Madison, WI 53706

1 Riccardo Bonazza
University of Wisconsin-Madison
1500 Engineering Drive
Madison, WI 53706

1 0747 Ben Cipiti, 6774